Preprints of the 21st IFAC World Congress (Virtual)
Berlin, Germany, July 12-17, 2020

Uncertainties Investigation and μ-Synthesis Control Design for a Full Car with Series Active Variable Geometry Suspension

Zilin Feng * **Min Yu** *** **Cheng Cheng** ** **Simos A. Evangelou** *
Imad M.Jaimoukha * **Daniele Dini** ***

* *Department of Electrical and Electronic Engineering, Imperial College London, London SW7 2AZ, UK (e-mail: zilin.feng17@imperial.ac.uk, s.evangelou@imperial.ac.uk, i.jaimouka@imperial.ac.uk)*
** *School of Artificial Intelligence and Automation, Huazhong University of Science and Techonology, Wuhan, 430074, China (e-mail: c_cheng@hust.edu.cn)*
*** *Department of Mechanical Engineering, Imperial College London, London SW7 2AZ, UK (e-mail: m.yu14@imperial.ac.uk, d.dini@imperial.ac.uk)*

Abstract: Linear robust control schemes, for example the H_∞ control, are commonly utilized in the control design of an active suspension system, with a linearized and time-invariant state-space model of the system adopted. However, the vehicle parameter uncertainties are mainly ignored and their effect on the control robustness is not investigated. In this paper, a μ-synthesis-based control scheme is synthesized for a full car with the recently introduced Series Active Variable Geometry Suspension (SAVGS), to mainly enhance the ride comfort and road holding performance, with two significant practical uncertainties in the sprung mass and the suspension damping taken into account. Numerical simulations with a high fidelity nonlinear vehicle model are performed, with the cases of the fixed and swept values of the sprung mass tested, to assess the control robustness and performance of the developed scheme against the passive suspension as well as the H_∞-controlled SAVGS. The proposed μ-synthesis control scheme is proved to be more effective for realistic applications as it is capable of maintaining the suspension performance improvement regardless of variations of system parameters associated with the uncertainties, while the H_∞ control performance tends to deteriorate when a notable deviation from the nominal values occurs.

Keywords: active suspension, robust control, μ-synthesis, uncertainties

1. INTRODUCTION

The conventional passive suspension system equipped with spring-damper (SD) units plays an important role in a car, as it isolates the vehicle's chassis from the road disturbances. In the past decades, with the increasing demand in more efficient systems and growing requirements in high-level ride comfort and road handling performance, innovative concepts of active suspension started to appear. The control methodologies of proportional-integral-derivative control and fuzzy logic control (Wang et al., 2012), model predictive control (Mehra et al., 1997), H_∞ control (Park and Kim, 1999), back-stepping (Yagiz and Hacioglu, 2008), sliding mode control and neural network control schemes (Al-Holou et al., 2002) have been considered and widely applied in active suspension systems.

Recently, a novel mechatronic suspension solution, the Series Active Variable Geometric Suspension (SAVGS), is proposed in (Arana, 2015). As shown in Fig. 1, in the SAVGS the active single-link component ('F-G') is in series with the end eye of the spring-damper unit ('F'), while the other end of this link ('G') is fixed on the chassis. A permanent magnet synchronous motor (PMSM), together with an epicyclic gearbox, attached on the chassis, are selected to drive the single link. As compared with other active suspensions, the SAVGS offers advantages in terms of: i) remarkable performance enhancement, ii) negligible unsprung mass and small sprung mass increments (Arana, 2015), iii) low power requirement, iv) safe operation and so on.

Previous work on the SAVGS consists of: i) the optimization of the single link geometric configuration as well as the actuation parameters, ii) the development of a nonlinear multi-body model for accurate numerical simulations, iii) PID-based low-frequency chassis attitude control (Arana et al., 2016) and H_∞-based high-frequency ride comfort and road holding improvement control (Arana et al., 2017), and iv) the practical validation of the SAVGS with a quarter car experimental study (Yu et al., 2017). However, despite these achievements, the previous work does not account for uncertainties of the sprung mass and the suspension damping in the control design, which may result in the deterioration of the SAVGS performance in the cases of increased payload (passengers and cargo), long

stroke operation of the suspension dampers (which have nonlinear characteristics), and so on.

In this paper, a μ-synthesis-based control scheme (Zhou and Doyle, 1998) is proposed with a linear equivalent model of the SAVGS full car, with the significant uncertainties of the sprung mass and the suspension damping considered. Numerical simulations with a high-fidelity SAVGS full car nonlinear model are further performed to evaluate the control robustness. The specific contributions of this paper are: i) the identification and characterization of structured uncertainties that are ignored during the linearization of the SAVGS full car, ii) the design of a μ-synthesis-based robust controller for the SAVGS, and iii) numerical simulations as well as comprehensive comparisons (of the SAVGS μ-synthesis control results with results of the H_∞-controlled SAVGS and the passive suspension cases) for the evaluation of the control robustness, with the uncertainties effect thoroughly investigated.

The rest of this paper is organized as follows. Section 2 describes the linearized model employed for the syntheses of robust control schemes and the nonlinear multi-body model utilized for the numerical simulations, and extracts significant uncertainties in the SAVGS operation. Section 3 designs a μ-synthesis control scheme with the identified uncertainties accommodated in the control framework. Section 4 performs numerical simulations to compare the μ-synthesis to the H_∞ control and the passive suspension case, given selected uncertainties, with the ride comfort and road holding being the primary indexes. Finally, conclusions are drawn in Section 5.

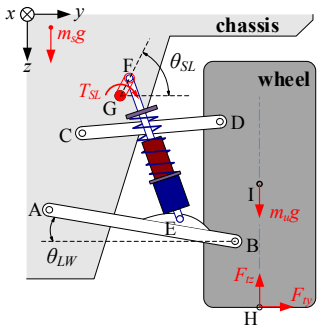

Fig. 1. SAVGS application to a quarter car double-wishbone suspension (Yu et al., 2017).

2. MATHEMATICAL MODELS AND UNCERTAINTIES INVESTIGATION

In this section, a high fidelity nonlinear multi-body full car model that is developed in (Arana, 2015) and that will be used for nonlinear simulations and evaluation of the sprung mass and the damper uncertainties, is summarized first. Following that, the linear equivalent model of the SAVGS full car derived in (Cheng, 2017) is stated and given in a state-space representation, to be utilised for the linear control synthesis (detailed later in section 3). Finally, the identification and characterization of the sprung mass and suspension damping uncertainties, resulting from actual system variance or approximations of nonlinear characteristics by linear counterparts, is provided.

2.1 Nonlinear multi-body full car model

The nonlinear multi-body model of the full car considered in the present work has been developed in (Arana, 2015) and it is briefly summarized here. The characteristics of the engine, powertrain, chassis, steering and breaking mechanism, and suspension system are mathematically described. Additionally, PI controllers are synthesized separately for closed-loop longitudinal and lateral control to implement ISO driving maneuvers (straight running at constant speed is considered in the present work). The main components of a nonlinear SAVGS model containing the single-link, and single-link driving actuator and gearbox, are further integrated into both the front and rear axles, to complete the SAVGS retrofit in the full car model. The SAVGS has previously been found to be especially suitable for GT (Grand Tourer) cars, therefore in the present work, representative parameter values of this vehicle category are used to populate the nonlinear multi-body model already mentioned. The major parameters of the GT car with SAVGS are given in Table 1.

Table 1. Main parameters of the nonlinear multi-body model of SAVGS full car

Parameter	Value
F/R Wheelbase (a_f/a_r)	1.5 m / 1.1 m
CMC Height (h_{CMC})	0.424 m
F/R Track (t_f/t_r)	1.669 m / 1.615 m
F/R suspension damping (c_{eqf}/c_{eqr})	1492.7 $\frac{Ns}{m}$ / 2028 $\frac{Ns}{m}$
F/R installation ratio (R_{SDf}/R_{SDr})	0.6/ 0.56
Nominal sprung mass (M_{nom})	1375 kg

'F/R' denotes Front/Rear

2.2 Linear equivalent model of SAVGS full car

To enable the linear robust control synthesis, a linear equivalent model of the SAVGS full car derived in (Cheng, 2017), as shown in the schematic of the full car in Fig. 2, is employed and summarized here. This model lumps the suspension geometric nonlinearities at each corner such that it continues to be accurate for a large range of operating conditions. Its state space representation can be obtained as follows:

$$\begin{aligned} \dot{\boldsymbol{x}} &= A\boldsymbol{x} + B\mathbf{v}, \\ \mathbf{o} &= C\boldsymbol{x} + D\mathbf{v}, \end{aligned} \tag{1}$$

where $\boldsymbol{x}^T = [\dot{z}_s, \dot{\theta}, \dot{\phi}, \dot{\boldsymbol{z}}_{\boldsymbol{u}}^T, \Delta\boldsymbol{l}_{\boldsymbol{s}}^T, \Delta\boldsymbol{l}_{\boldsymbol{t}}^T, \boldsymbol{z}_{\boldsymbol{lin}}]$ is the system state, in which: a) $\dot{z}_s$ is CMC (center of the mass of the chassis) vertical velocity, b) $\dot{\theta}$ and $\dot{\phi}$ are pitch and roll velocities of the chassis respectively, c) $\dot{\boldsymbol{z}}_{\boldsymbol{u}} = [\dot{z}_{u1}, \dot{z}_{u2}, \dot{z}_{u3}, \dot{z}_{u4}]^T$ are the vertical velocities of the unsprung masses (m_u) at each wheel, d) $\Delta\boldsymbol{l}_{\boldsymbol{s}} = [\Delta l_{s1}, \Delta l_{s2}, \Delta l_{s3}, \Delta l_{s4}]^T$ are the suspension deflections at the four corners (for example, $\Delta l_{s1} = z_{u1} - z_1$, where z_1 is calculated from z_s, θ, ϕ, α_f, and $t_f/2$), e) $\Delta\boldsymbol{l}_{\boldsymbol{t}} = [\Delta l_{t1}, \Delta l_{t2}, \Delta l_{t3}, \Delta l_{t4}]^T$ are the tire deflections at each corner (for example, $\Delta l_{t1} = z_{r1} - z_{u1}$), and f) $\boldsymbol{z}_{\boldsymbol{lin}} = [z_{lin1}, z_{lin2}, z_{lin3}, z_{lin4}]^T$ are the linear equivalent actuator displacements at each corner. The system input includes the disturbance signals and control input, which is defined as: $\mathbf{v}^T = [\mathbf{w}^T, \mathbf{u}^T]$ where the exogenous disturbance signal is $\mathbf{w} = [\dot{\boldsymbol{z}}_{\boldsymbol{r}}^T, T_p, T_r]^T$ and the control input is $\mathbf{u} = \dot{\boldsymbol{z}}_{\boldsymbol{lin}}$, in

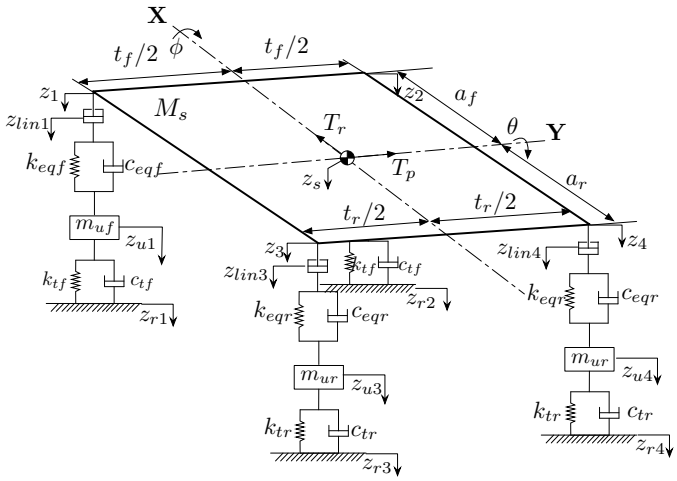

Fig. 2. Linear equivalent model of SAVGS full car (Cheng, 2017; Yu et al., 2019)

which $\dot{\boldsymbol{z}}_{\boldsymbol{r}} = [\dot{z}_{r1}, \dot{z}_{r2}, \dot{z}_{r3}, \dot{z}_{r4}]^T$ are the derivatives of the road (displacement) profiles at the four wheels, T_p and T_r are respectively the exogenous pitch and roll torques applied on the chassis, and $\dot{\boldsymbol{z}}_{\boldsymbol{lin}} = [\dot{z}_{lin1}, \dot{z}_{lin2}, \dot{z}_{lin3}, \dot{z}_{lin4}]^T$ are the derivatives of the linear equivalent actuator displacements. The selection of the vector of output variables, $\mathbf{o}$, is based on the the sensors availability as:

$$\mathbf{o}^T = [\boldsymbol{z}_{\boldsymbol{lin}}^T, \Delta\boldsymbol{l}_{\boldsymbol{t}}^T, \Delta\boldsymbol{l}_{\boldsymbol{s}}^T, \ddot{z}_s, \ddot{\theta}, \ddot{\phi}], \tag{2}$$

where the last three variables are derivatives of variables already introduced.

In addition, as shown in Fig. 3, conversion functions α (from each $\dot{z}_{lin}$ to the rotational velocity of the corresponding single link, $\dot{\theta}_{SL}$) that are associated with the suspension geometric nonlinearity, are further considered to bridge the linear equivalent and nonlinear multi-body models of the SAVGS full car (Yu et al., 2019).

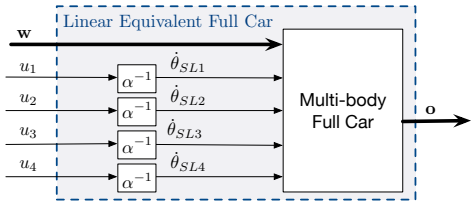

Fig. 3. Conversion between linear equivalent and multi-body models of the SAVGS full car.

2.3 Uncertainties represented in full car linearisation

Uncertainties represent the discrepancy between the model used to design the controller and the actual system.

With respect to the SAVGS full car, the most significant and typical structured uncertainties include the sprung mass (M_s), and the suspension damping (c_{eqf}, c_{eqr}) for the front and rear axle spring-damper units respectively. The M_s parameter variation is due to weight change in passenger load and/or cargo. In the present work $M_{\text{nom}} = 1375\,\text{kg}$ is the nominal sprung mass (one male passenger) and $M_{max} = 1525\,\text{kg}$ is the maximum sprung mass (two overweight male passengers). The variation of c_{eqf} and c_{eqr} is mainly caused by the considerable operational speed range of the dampers, which have nonlinear speed-dependent characteristics. The nonlinear characteristics of the actual dampers employed in this work are shown in Fig. 4. The aim of the linearized characteristics utilized in the linear equivalent model, and also shown in Fig. 4, are to provide the optimal compromise between the maximum and minimum slopes of the respective nonlinear characteristics (Arana, 2015; Cheng, 2017; Yu et al., 2017). The present work represents the nonlinear damper as a nominal linear counterpart plus uncertainty. The possible ranges of values for the uncertain parameters are thus given as:

$$\begin{aligned} M_s &= (\bar{M}_s + \delta M_s)\,\text{kg}, \\ c_{eqf} &= (\bar{c}_{eqf} + \delta c_{eqf})\,\text{Ns/m}, \\ c_{eqr} &= (\bar{c}_{eqr} + \delta c_{eqr})\,\text{Ns/m}, \end{aligned} \tag{3}$$

where $\bar{M}_s = 1375\,\text{kg}$, $\bar{c}_{eqf} = 1492.7\,\text{Ns/m}$ and $\bar{c}_{eqr} = 2028\,\text{Ns/m}$. The perturbation parameters δM_s, δc_{eqf} and δc_{eqr} are defined as follows:

$$\begin{aligned} \delta M_s &\in [0, 0.11\,\bar{M}_s], \\ \delta c_{eqf} &\in [-0.3\,\bar{c}_{eqf}, 0.3\,\bar{c}_{eqf}], \\ \delta c_{eqr} &\in [-0.3\,\bar{c}_{eqr}, 0.3\,\bar{c}_{eqr}]. \end{aligned} \tag{4}$$

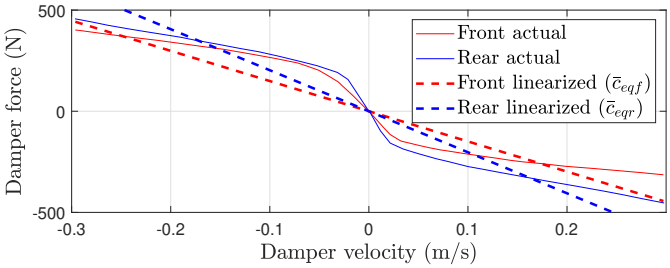

Fig. 4. Nonlinear (solid) and linearized (dashed) characteristics of damper force versus damper velocity for the damper units installed at the front (red) and rear (blue) axles (Cheng, 2017).

3. ROBUST CONTROL DESIGN

This section synthesizes a μ-synthesis control scheme based on the linear equivalent model, with the ride comfort and road holding enhancement being the main objectives. It is also desired to stabilize each of the SL angles at the desired value in low-frequency cases (or at the nominal angle offset in steady-state) (Arana, 2015; Cheng and Evangelou, 2019), and maintain a reasonable level of control effort. For numerical simulation comparison (in Section 4) purposes, the design of a conventional H_∞ controller, using the same linear equivalent model and addressing the same objectives (Cheng and Evangelou, 2019), is also summarized first in this section.

3.1 Generalized regulator for H_∞ control synthesis

The generalized regulator, shown in Fig. 5 is directly utilized in the H_∞ control synthesis and can be further developed to enable the μ synthesis.

The H_∞ control framework is used to synthesize controllers that achieve stabilization with guaranteed performance. As shown in Fig. 5, it intends to find a controller K such that the influence of exogenous disturbance ($\mathbf{w}$) to system performance objectives ($\tilde{\mathbf{z}}$) is minimized according

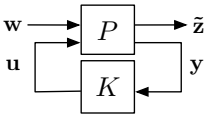

Fig. 5. Generalised regulator. P corresponds to a time-invariant state-space representation of a linear plant, K to the synthesized controller, $\mathbf{w}$ to exogenous disturbance signals, $\tilde{\mathbf{z}}$ to the cost signals to be minimized, $\mathbf{u}$ to manipulated variables, and $\mathbf{y}$ to the measurements feedback.

to the H_∞ norm. The closed-loop transfer function matrix $F_l(P,K)$ infinity norm is defined as:

$$\|F_l(P,K)\|_\infty = \sup_\omega \bar{\sigma}\left(F_l(P,K)(j\omega)\right), \tag{5}$$

where $\bar{\sigma}$ is the maximum singular value in the frequency domain. The H_∞ control design process involves the use of frequency-dependent weighting functions to tune the performance according to the ride comfort and road holding requirements.

Figure 6 shows the closed-loop structure augmented with frequency weights for the H_∞ control synthesis ($P_\mathbf{w}$ is the augmented linear equivalent full car model, P), with disturbance signals, cost signals, manipulated variables, and measurements defined subsequently in (6)-(11).

The unweighted exogenous disturbance signals are defined as follows:

$$\tilde{\mathbf{w}} = [\tilde{\mathbf{w}}_\mathbf{a}, \tilde{\mathbf{w}}_\mathbf{b}] = [\tilde{\mathbf{w}}_\mathbf{I}, \tilde{\mathbf{w}}_\mathbf{II}, \tilde{w}_9, \tilde{w}_{10}, \tilde{\mathbf{w}}_\mathbf{III}, \tilde{w}_{15}, \tilde{w}_{16}, \tilde{w}_{17}]^T, \tag{6}$$

in which,

$$\tilde{\mathbf{w}}_\mathbf{a}^T = [\tilde{\mathbf{w}}_\mathbf{I}, \tilde{\mathbf{w}}_\mathbf{II}, \tilde{w}_9, \tilde{w}_{10}] = [(\mathbf{z}_\mathbf{lin}^{(\mathbf{e})})^T, \dot{\boldsymbol{z}}_\boldsymbol{r}^T, T_p, T_r], \tag{7}$$

where $\mathbf{z}_\mathbf{lin}^{(\mathbf{e})} = [z_{lin1}^{(e)}, z_{lin2}^{(e)}, z_{lin3}^{(e)}, z_{lin4}^{(e)}]^T$ are the exogenous commands of the linear equivalent actuator displacements, and

$$\tilde{\mathbf{w}}_\mathbf{b}^T = [\tilde{\mathbf{w}}_\mathbf{III}, \tilde{w}_{15}, \tilde{w}_{16}, \tilde{w}_{17}], \tag{8}$$

with $\tilde{\mathbf{w}}_\mathbf{III}$ corresponding to the suspension deflection sensor noise signals, and $\tilde{w}_{15}$, $\tilde{w}_{16}$ and $\tilde{w}_{17}$ to the CMC vertical, chassis pitch and chassis roll acceleration sensor noise signals.

The unweighted cost signal $\tilde{\mathbf{z}}$ is defined as follows:

$$\tilde{\mathbf{z}}^T = [(\dot{\boldsymbol{z}}_{\boldsymbol{lin}}^*)^T, \boldsymbol{e}_{\boldsymbol{z}_{lin}}^T, \boldsymbol{\Delta l}_\boldsymbol{t}^T, \ddot{z}_s, \ddot{\theta}, \ddot{\phi}], \tag{9}$$

where $\dot{\boldsymbol{z}}_{\boldsymbol{lin}}^*$ are the equivalent actuator reference speeds and $\boldsymbol{e}_{\boldsymbol{z}_{lin}} = \mathbf{z}_\mathbf{lin}^{(\mathbf{e})} - \boldsymbol{z}_{\boldsymbol{lin}}$ are the tracking errors of the linear equivalent actuator displacement.

The measurement signal $\mathbf{y}$ is defined as:

$$\mathbf{y}^T = [\mathbf{y}_\mathbf{I}, \mathbf{y}_\mathbf{II}, y_9, y_{10}, y_{11}] = [\boldsymbol{e}_{\boldsymbol{z}_{lin}}^T, \boldsymbol{\Delta l}_\boldsymbol{s}^T, \ddot{z}_s, \ddot{\theta}, \ddot{\phi}], \tag{10}$$

and the unweighted control signal $\tilde{\mathbf{u}}$ fed to the plant is defined as:

$$\tilde{\mathbf{u}} = \dot{\boldsymbol{z}}_{\boldsymbol{lin}}^*. \tag{11}$$

The unweighted signals already defined ($\tilde{\mathbf{w}}$, $\tilde{\mathbf{z}}$, and $\tilde{\mathbf{u}}$) are weighted by constant or frequency-dependent weighting functions, which are carefully tuned to achieve the desired performance objectives. The weighting functions, described next, are parameterized in terms of their DC gain and cut-off frequencies, which scale the importance level between different objectives and filter the signals at their frequencies of interests, respectively.

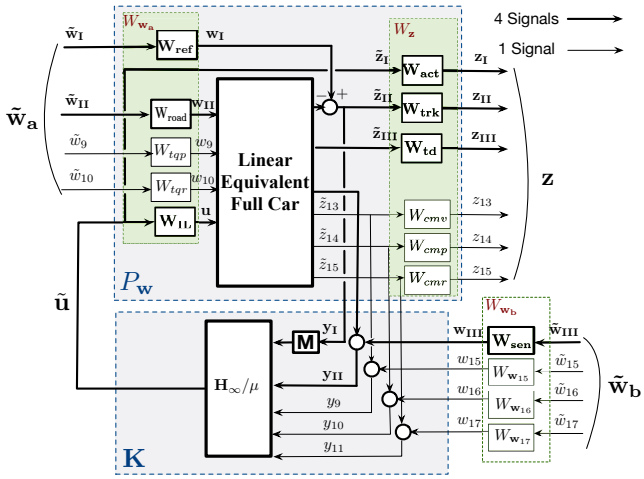

Fig. 6. Interconnection for H_∞ control, where the signals and blocks are explained in (6)-(15).

Selection of input weighting functions Input weights are related to the maximum expected value of the input signals, $\tilde{\mathbf{w}}$ and $\tilde{\mathbf{u}}$, shown in Fig. 6. The constant weights selected for road height rate changes, and pitch and roll torques are:

$$\begin{aligned} W_{road,\,i} &= 0.25, \quad i = 1,\ldots,4, \\ W_{tqp} &= 4050, \; W_{tqr} = 2700, \end{aligned} \tag{12}$$

where $i = 1,\ldots,4$ represents the index of each vehicle corner, in the order: front left, front right, rear left and rear right. The frequency-dependent weights for exogenous references of the linear equivalent actuator displacements are selected as low pass filters with 1 Hz cut-off frequency and the DC gain is obtained by the their maximum value ($\approx 0.02\,\mathrm{m}$), related to the maximum single-link rotation ($\theta_{SL} = 0°$ or $180°$). Hence, the weights for the exogenous linear equivalent actuator displacements references are defined as:

$$W_{ref,\,i} = 0.02 \cdot \frac{1}{\frac{1}{(2\pi\cdot 1)}s + 1}, \quad i = 1,\ldots,4. \tag{13}$$

Weighting functions for sensor noise, $W_{w_{15}}$, $W_{w_{16}}$, $W_{w_{17}}$, and $\mathbf{W_{sen}}$, are designed to account for the noise spectrum of the chassis acceleration and suspension deflection (displacement) sensors, which are:

$$\begin{aligned} W_{w_j} &= 0.5, \quad j = 15, 16, 17, \\ W_{sen,\,i} &= 0.01, \quad i = 1,\ldots,4. \end{aligned} \tag{14}$$

Since the rapid change of the single-link angular velocity cannot be accurately tracked beyond a certain frequency (18 Hz), based on actuator limitations, a first-order transfer function is introduced to represent the nominal dynamics of the single-link actuators:

$$W_{IL,\,i} = \frac{1}{\frac{1}{(2\pi\cdot 17.8)}s + 1}, \quad i = 1,\ldots,4. \tag{15}$$

Selection of output weighting functions The output weights applied on the cost signals, $\tilde{\mathbf{z}}$, are chosen to shape the performance and objectives. $W_{act,\,i}$ are defined as high pass filters to penalise the high-frequency components of the linear equivalent actuator speeds and restrict the control bandwidth of the actuators:

$$W_{act,\,i} = \frac{1}{6.49} \cdot \frac{\frac{1}{(2\pi\cdot 10)^2}s^2 + \frac{2}{2\pi\cdot 10}s + 1}{\frac{1}{(2\pi\cdot 100)^2}s^2 + \frac{2}{2\pi\cdot 100}s + 1}, \quad i = 1, \ldots, 4. \tag{16}$$

$W_{trk,\,i}$ are defined as low pass filters, which ensure that the SL angles track the command positions at low or zero frequencies, without overlapping with the frequency ranges (2-10 Hz) of other higher frequency objectives, such as the control of chassis accelerations and tire deflections:

$$W_{trk,\,i} = 0.006 \cdot \frac{\frac{1}{(2\pi\cdot 120)}s + 1}{\frac{1}{(2\pi\cdot 0.3)}s + 1}, \quad i = 1, \ldots, 4. \tag{17}$$

In terms of the main control objectives, the cut-off frequencies of the ride comfort weighting functions, W_{cmv}, W_{cmp}, and W_{cmr}, are selected to be 5 Hz, 0.8 Hz, and 1 Hz respectively, according to the human body sensitivity to vibrations (ISO, 1997). Road holding weights, W_{tdi}, are chosen as band pass filters to penalise the road disturbances within 1-5 Hz:

$$\begin{aligned} W_{cmv} &= \frac{7}{\frac{1}{(2\pi\cdot 5)}s + 1}, \; W_{cmp} = \frac{4.5}{\frac{1}{(2\pi\cdot 0.8)}s + 1}, \\ W_{cmr} &= \frac{1.45}{\frac{1}{(2\pi\cdot 1)}s + 1}, \\ W_{td3} &= W_{td4} = 2W_{td1} = 2W_{td2} = \frac{\frac{1.2}{(2\pi\cdot 0.001)}s + 1.2}{\frac{1}{(2\pi)^2\cdot 5}s^2 + \frac{4}{2\pi\cdot 3} + 1}. \end{aligned} \tag{18}$$

In addition, the integrator blocks (block $\mathbf{M}$ in Fig. 6) are included to obtain a zero tracking error for the linear equivalent actuator displacement:

$$M_i = \frac{1}{s}, \quad i = 1, \ldots, 4. \tag{19}$$

With the tuned input and output weighting functions, the H_∞ control scheme can be synthesized by using the MATLAB command `hinfsyn`. However, H_∞ control only deals with the problem of finding a controller for a known system and produces more conservative controllers that might not be able to meet the design specifications. μ-synthesis extends the H_∞ control to the case when the system is uncertain and minimizes the worst-case gain given the uncertainty description. Additionally, by using μ-synthesis, the performance of the system can be further improved while still satisfying the requirements that the induced disturbances from the uncertainty remain below a certain level.

3.2 μ-synthesis control

The μ-synthesis control allows to design a multi-variable optimal robust controller for complex linear systems with any type of uncertainty in their structure, such as structured or unstructured uncertainty. As shown in Fig. 7, the objective of μ-synthesis is to calculate a robust controller for the uncertain open-loop plant model via the *D-K* algorithm (Zhou and Doyle, 1998). In the present work, the variations of the sprung mass and suspension damping are possible to characterize as structured uncertainties, thus unstructured uncertainties are not involved.

The system N in Fig. 7 is defined as follows:

$$N(s) = F_l(P(s), K(s)) = \begin{bmatrix} N_{11}(s) & N_{12}(s) \\ N_{11}(s) & N_{22}(s) \end{bmatrix}, \tag{20}$$

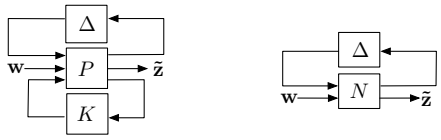

(a) (b)

Fig. 7. (*a*) Extended generalized regulator for μ-synthesis, and (*b*) analysis framework (Zhou and Doyle, 1998). Δ is a structured uncertainty block diagonal matrix.

where F_l denotes a lower linear fractional transform of control plant P and robust controller K.

Then the general framework is reduced to Fig. 7(*b*), and the formulation becomes:

$$\tilde{\mathbf{z}} = F_u(N, \Delta)\cdot\mathbf{w} = [N_{22} + N_{21}\Delta(I - N_{11}\Delta)^{-1}N_{12}]\cdot\mathbf{w}, \tag{21}$$

where the upper linear fractional transformation, $F_u(N, \Delta)$, is the closed-loop system from exogenous disturbance ($\mathbf{w}$) to cost signals ($\tilde{\mathbf{z}}$) to be minimized.

The structured singular value, μ, is used to evaluate robust stability and performance of a system, N. Mathematically,

$$\mu(N)^{-1} \triangleq \min_{\Delta} \{\bar{\sigma}(\Delta) | det(I - N\Delta) = 0\}, \tag{22}$$

in which μ is defined as the inverse of the largest singular value $\bar{\sigma}$, and Δ is a structured uncertainty block diagonal matrix, which in the present work is defined as:

$$\Delta = \begin{bmatrix} \delta M_s & 0 & 0 \\ 0 & \delta c_{eqf} & 0 \\ 0 & 0 & \delta c_{eqr} \end{bmatrix}, \tag{23}$$

where the perturbation parameters δM_s, δc_{eqf} and δc_{eqr} are defined previously in (4). Δ is obtained to make the system N marginally stable.

In μ-synthesis control, the *D-K* iteration method integrates two optimization problems and solves them by fixing either the variable $F(s)$ or the variable $D(s)$ by utilising H_∞ control and μ-synthesis approaches respectively. The upper bound of μ is given by:

$$\mu(N) \leq \min_{D\in\mathcal{D}} \bar{\sigma}(DND^{-1}), \tag{24}$$

where $\mathcal{D}$ is the scaling set of nonlinear matrices (D) that satisfy $D\Delta = \Delta D$ (Zhou and Doyle, 1998). The control problem is to find a controller that minimizes this aforementioned upper bound, which means solving the double minimization given by:

$$\min_K \left(\min_{D\in\mathcal{D}} \left\| DN(K)D^{-1} \right\|_\infty \right). \tag{25}$$

The minimization is solved alternately with respect to K and D. The D matrix is initialised to a transfer matrix with appropriate structure (i.e. identity matrix) and the *D-K* iteration algorithm is summed by the following steps:

i. Fix the matrix $D(s)$, and the H_∞-optimal controller $K(s)$ that minimizes γ can be synthesized:

$$\gamma = \min_K \left\| DN(K)D^{-1} \right\|_\infty. \tag{26}$$

ii. Hold $K(s)$ obtained from step i fixed and solve the following minimization problem for $D(j\omega)$ at each frequency:

$$\min_D \bar{\sigma}(DN(K(s))D^{-1}). \tag{27}$$

iii. Construct a minimum phase system transfer function $D(s)$ by using the magnitude of the elements of $D(j\omega)$ and go to step i.

The stopping criteria of the D-K iteration are when $\left\|DN(K)D^{-1}\right\|_\infty \leq 1$ is met, or $\left\|DN(K)D^{-1}\right\|_\infty$ reaches its minimum value.

The interconnection and weights for the H_∞ control synthesis shown in Fig. 6 are applicable for the μ-synthesis as well. The weighting function parameter values chosen for the H_∞ control synthesis in Section 3.1 are found to be beneficial and applied to the μ-synthesis also.

To perform a comprehensive comparison to synthesized H_∞ controller, three different μ-synthesis controllers are designed by means of the MATLAB command `dksyn`, with accommodating: i) only the sprung mass uncertainty (μ_{mass}), ii) only the suspension damping uncertainty ($\mu_{damping}$), and iii) both the sprung mass and the suspension damping uncertainties ($\mu_{combined}$).

4. NUMERICAL SIMULATIONS AND ANALYSIS

In this section, numerical simulations are performed with the nonlinear multi-body model (described in Section 2.1) with a forward speed of 100 km/h, a nominal angle offset of $\theta_{SL} = 90°$ and a maximum driving power of 500 W for each SL actuator. The performance of the μ-synthesis controllers proposed in Section 3.2 is tested with the nonlinear full-car model for a random road profile (as defined in (ISO, 2016). For comparison purposes, the passive and H_∞-controlled multi-body model cases are also simulated. The road profile is usually described in terms of its power spectral density (PSD):

$$G_d(n) = 10^{-6} \cdot 2^{2k} \left(\frac{n}{n_0}\right)^{-\hat{\omega}}, \tag{28}$$

where n is the spatial frequency, $n_0 = 0.1$ cycles/m and $\hat{\omega} = 2$ are constants, whereas $k = 2$ to 9 represents road roughness classes A to H respectively. In the present work, Class C road is selected for simulation which corresponds to a poor quality road surface to better validate the improvement of the ride comfort and road holding.

Numerical simulations are performed to evaluate two aspects of performance: the benefits of accounting for the suspension damping nonlinearity (aspect A) and for the sprung mass variation due to payload changes (aspect B) as parametric uncertainties in the linear control synthesis. Three simulation cases are performed, each with a different case of sprung mass, M_s: a) nominal sprung mass ($M_s = M_{\text{nom}}$) to evaluate aspect A, b) maximum sprung mass ($M_s = M_{\max}$) to evaluate both aspects A and B, and c) swept sprung mass ($M_s = M_{\text{nom}}$ to $M_{\max}$) to evaluate aspect B. The ride comfort related variables of the CMC vertical acceleration ($\ddot{z}_s$), the chassis pitch ($\ddot{\theta}_s$) and roll ($\ddot{\phi}_s$) accelerations, and the road holding related variables of the tire deflections (Δl_{ti}) are considered as the evaluation indexes.

4.1 Evaluation of aspect A (nominal sprung mass)

The PSD plots of $\ddot{z}_s$, $\ddot{\theta}_s$ and $\ddot{\phi}_s$, and Δl_{t1} and Δl_{t3} in the case of $M_s = M_{\text{nom}}$ are shown in Figs. 8 and 9 respectively, and their root mean square (RMS) and peak-to-peak (PTP) values in the time domain are listed in Tables 2 and 3 respectively. Due to the symmetry of the chassis geometry, the responses of Δl_{t2} and Δl_{t4} are respectively similar to those of Δl_{t1} and Δl_{t3}, and are not shown here. It can be seen that the ride comfort and the road holding are significantly improved by all the active control cases as compared to the passive system, while the μ-synthesis controller μ_{mass} has nearly the same performance as that of the H_∞ controller (for example, 6 dB reduction at 2 Hz in the case of CMC vertical acceleration, with respect to the passive system) as would be expected;

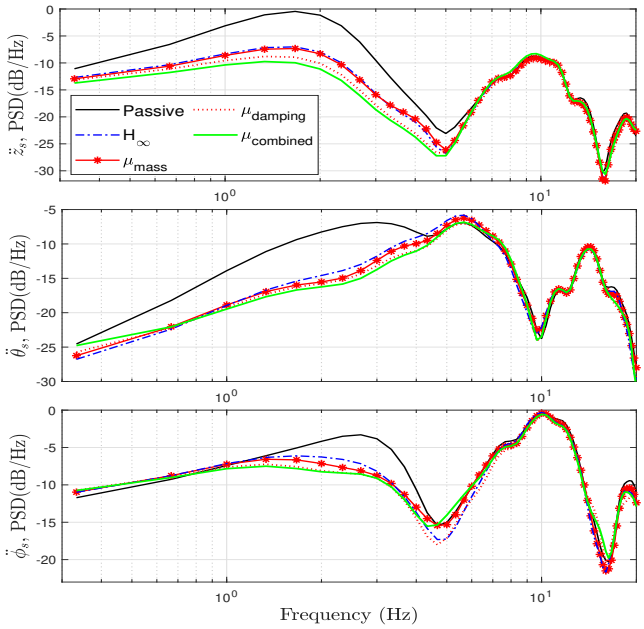

Fig. 8. Numerical simulation results in the case of $M_s = M_{\text{nom}}$: the PSD of $\ddot{z}_s$, $\ddot{\theta}_s$ and $\ddot{\phi}_s$ with the H_∞ and different μ-synthesis controllers.

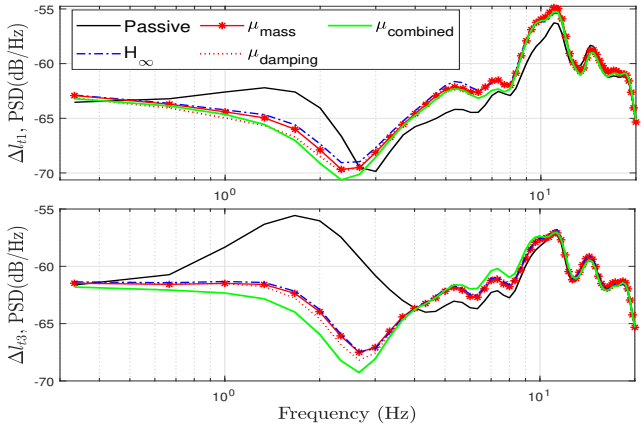

Fig. 9. Numerical simulation results in the case of $M_s = M_{\text{nom}}$: the PSD of Δl_{t1} and Δl_{t3} with the H_∞ and different μ-synthesis controllers.

in this simulation there is no variation of the sprung mass from its nominal value and neither of the H_∞ and μ_{mass} controllers take the suspension damping uncertainty into account. In contrast, the $\mu_{damping}$ and $\mu_{combined}$ controllers, which both account for the damping uncertainty, achieve a better performance than the H_∞ controller. This

can be observed in all the PSD plots in Figs. 8 and 9 in the range 1-4 Hz, especially in the case of $\ddot{z}_s$ for which they achieve a reduction of 9 dB and 10 dB respectively at 2Hz, as compared to the passive case, and consequently 3-4 dB reduction as compared to the H_∞ control case. The improvement offered by $\mu_{combined}$ over the passive and H_∞ controller cases, in terms of time-domain RMS and peak-to-peak values, is further observed in Tables 2 and 3.

Table 2. RMS and peak-to-peak values of the $\ddot{z}_s$, $\ddot{\theta}_s$ and $\ddot{\phi}_s$ with different controllers, $M_s = M_{\text{nom}}$

	Parameter	Passive	H_∞	$\mu_{combined}$
RMS	$\ddot{z}_s$	1.3603	0.9507(-30%)	0.8932(-34%)
	$\ddot{\theta}_s$	1.1694	1.0768(-8%)	1.0051(-14%)
	$\ddot{\phi}_s$	2.4712	2.3030(-8%)	2.2106(-10%)
PTP	$\ddot{z}_s$	3.8553	2.7168(-29%)	2.5445(-34%)
	$\ddot{\theta}_s$	2.7243	2.5107(-8%)	2.2595(-17%)
	$\ddot{\phi}_s$	7.1284	6.5581(-8%)	6.3443(-11%)

Table 3. RMS and peak-to peak values of the Δl_{t1} and Δl_{t3} with different controllers, $M_s = M_{\text{nom}}$

	Parameter	Passive	H_∞	$\mu_{combined}$
RMS	$\lvert\Delta l_{t1}\rvert$	0.0043	0.0043(+0%)	0.0044(+2%)
	$\lvert\Delta l_{t3}\rvert$	0.0046	0.0044(-4%)	0.0042(-8%)
PTP	$\lvert\Delta l_{t1}\rvert$	0.0146	0.0149(+2%)	0.0140(+4%)
	$\lvert\Delta l_{t3}\rvert$	0.0143	0.0139(-3%)	0.0130(-9%)

4.2 Evaluation of both aspects A and B (maximum sprung mass)

Figures 10 and 11 illustrate the PSDs of $\ddot{z}_s$, $\ddot{\theta}_s$ and $\ddot{\phi}_s$, and Δl_{t1} and Δl_{t3} in the case of $M_s = M_{\text{max}}$. As it can be seen, in this case the performance improvement of the H_∞ scheme as compared to the passive system (for example, 4.3 dB reduction at 2 Hz in terms of CMC vertical acceleration) is not as great as when $M_s = M_{\text{nom}}$ (see Section 4.1), due to the lack of robustness of this scheme to variations in the sprung mass. However, in the case of $M_s = M_{\text{max}}$ both the uncertainties of the sprung mass and the suspension damping are presented; for increased M_s the damper is forced to operate in a wider range of damper speeds, whereby the damper experiences more nonlinear behavior. As such, significant reductions are clearly observed for the μ_{mass} controller (-7.3 dB at 2 Hz for $\ddot{z}_s$ as compared to the passive case), and for the $\mu_{damping}$ controller (-8.7 dB at 2 Hz for $\ddot{z}_s$ as compared to the passive case). The best attenuation of all control schemes is achieved by the $\mu_{combined}$ controller (-10 dB at 2 Hz for $\ddot{z}_s$ as compared to the passive case). Similar conclusions can be drawn from the time domain comparison of RMS and peak-to-peak values of the passive, H_∞-controlled and $\mu_{combined}$-controlled systems, as shown in Tables 4 and 5.

Time histories of $\ddot{z}_s$ for the passive and two cases of controlled system are presented in Fig. 12. It can be seen that the H_∞ controller attenuates $\ddot{z}_s$ considerably as compared to the passive case, while the $\mu_{combined}$ controller provides further enhancement over the H_∞ controller.

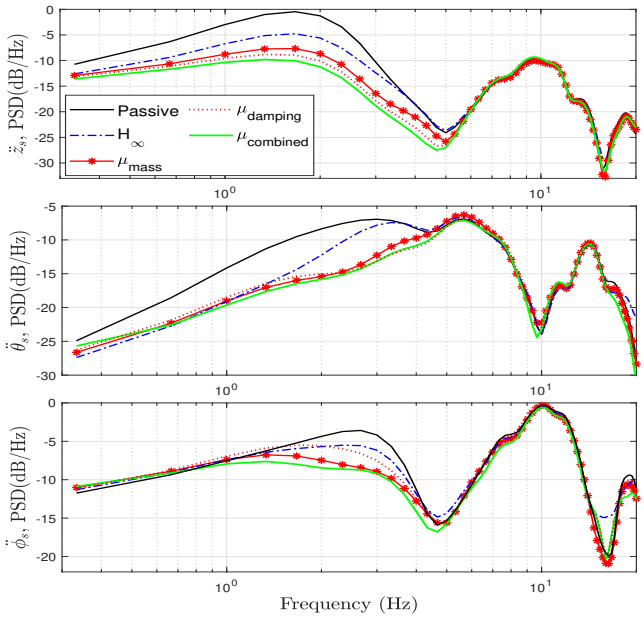

Fig. 10. Numerical simulation results in the case of $M_s = M_{\text{max}}$: the PSD of $\ddot{z}_s$, $\ddot{\theta}_s$ and $\ddot{\phi}_s$ with the H_∞ and different μ-synthesis controllers.

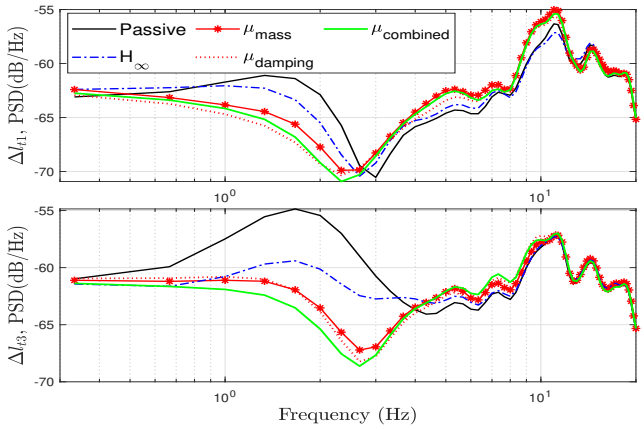

Fig. 11. Numerical simulation results in the case of $M_s = M_{\text{max}}$: the PSD of Δl_{t1} and Δl_{t3} with the H_∞ and different μ-synthesis controllers.

Table 4. RMS and peak-to-peak values of the $\ddot{z}_s$, $\ddot{\theta}_s$ and $\ddot{\phi}_s$ with different controllers, $M_s = M_{\text{max}}$

	Parameter	Passive	H_∞	$\mu_{combined}$
RMS	$\ddot{z}_s$	1.3692	1.0680(-22%)	0.8218(-37%)
	$\ddot{\theta}_s$	1.1672	1.0971(-6%)	1.0472(-10%)
	$\ddot{\phi}_s$	2.4602	2.3340(-5%)	2.2703(-8%)
PTP	$\ddot{z}_s$	3.6165	2.8967(-20%)	2.2944(-37%)
	$\ddot{\theta}_s$	2.6946	2.5781(-4%)	2.4103(-11%)
	$\ddot{\phi}_s$	7.0830	6.8417(-3%)	6.4502(-9%)

Table 5. RMS and peak-to-peak values of the Δl_{t1} and Δl_{t3} with different controllers, $M_s = M_{\text{max}}$

	Parameter	Passive	H_∞	$\mu_{combined}$
RMS	$\lvert\Delta l_{t1}\rvert$	0.0043	0.0043(+0%)	0.0044(+2%)
	$\lvert\Delta l_{t3}\rvert$	0.0046	0.0044(-4%)	0.0042(-8%)
PTP	$\lvert\Delta l_{t1}\rvert$	0.0146	0.0149(+2%)	0.0140(+4%)
	$\lvert\Delta l_{t3}\rvert$	0.0143	0.0139(-3%)	0.0130(-9%)

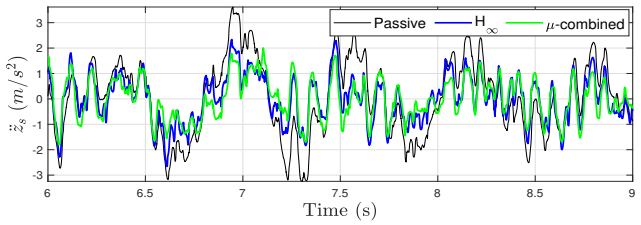

Fig. 12. Numerical simulation results in the case of $M_s = M_{\max}$: $\ddot{z}_s$ time histories for the passive, H_∞-controlled and $\mu_{combined}$-controlled systems.

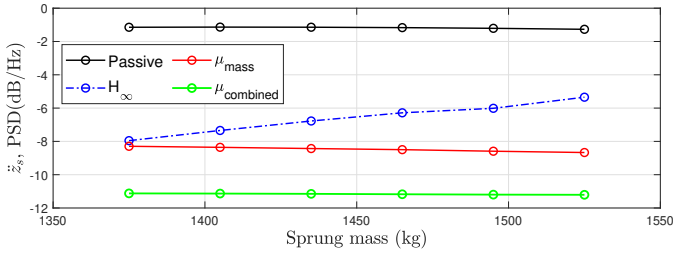

Fig. 13. The PSD gain of $\ddot{z}_s$ at the frequency of 2 Hz for different values of M_s (swept from M_{nom} to $M_{\max}$ in 30 kg increments). The passive system, and H_∞ and different μ-synthesis control performances are compared.

4.3 Evaluation of aspect B (swept sprung mass)

Figure 13 shows the PSD values of the $\ddot{z}_s$ at the fixed frequency of 2 Hz for M_s swept from M_{nom} to $M_{\max}$ in steps of 30 kg. Thus, the ride comfort performance difference between the H_∞ and two μ-synthesis controllers (μ_{mass} and $\mu_{combined}$), as the sprung mass is varied, is indicated. As compared to the passive case and for the whole M_s range, the μ-combined controller maintains the largest ride comfort performance enhancement (-10 dB), followed by the μ_{mass} controller (-7 dB). The H_∞ controller achieves the least improvement over the passive case and becomes less performing as M_s increases; it has the same performance as with the μ_{mass} scheme of -7 dB at $M_s = M_{\text{nom}}$, deteriorating almost linearly to -4 dB when $M_s = M_{\max}$. These results illustrate the improved robustness of the μ-synthesis control schemes as compared to the H_∞ scheme, for variations in the sprung mass.

5. CONCLUSION

The control for ride comfort and road holding performance enhancement of a full car with the series active variable geometry suspension (SAVGS) is investigated, with uncertainties of the sprung mass and suspension damping taken into account. A linear equivalent model is utilized to design linear robust controllers using H_∞ and μ-synthesis frameworks, which are then simulated with a representative high-fidelity nonlinear full car multi-body model. Selected uncertainties of the suspension damping (representing the damper characteristic nonlinearity) and sprung mass are considered in the μ-synthesis design process. Essential improvement over the passive suspension system case can be observed with the H_∞ controller, in terms of both ride comfort and road holding. Moreover, the μ-synthesis controller realizes significant enhancement over the H_∞ controller performance, especially when the sprung mass rises well above its nominal value due to increased mass of cargo or passengers. The results demonstrate the effective robustness of the μ-synthesis control framework and its suitability for realistic applications of the SAVGS.

REFERENCES

Nizar Al-Holou, Tarek Lahdhiri, Dae Sung Joo, Jonathan Weaver, and Faysai Al-Abbas. Sliding mode neural network inference fuzzy logic control for active suspension systems. *IEEE Transactions on Fuzzy Systems*, 10(2): 234–246, 2002.

Carlos Arana. *Active variable geometry suspension for cars*. PhD thesis, Imperial College London, 2015.

Carlos Arana, Simos A Evangelou, and Daniele Dini. Series active variable geometry suspension application to chassis attitude control. *IEEE/ASME Transactions on Mechatronics*, 21(1):518–530, 2016.

Carlos Arana, Simos A Evangelou, and Daniele Dini. Series active variable geometry suspension application to comfort enhancement. *Control Engineering Practice*, 59:111–126, 2017.

Cheng Cheng. *Control Strategies of Series Active Variable Geometry Suspension for Cars*. PhD thesis, Imperial College London, 2017.

Cheng Cheng and Simos A Evangelou. Series active variable geometry suspension robust control based on full-vehicle dynamics. *Journal of Dynamic Systems, Measurement, and Control*, 141(5):051002, 2019.

ISO. 2631-1:1997, Mechanical vibration and shock - Evaluation of human exposure to whole-body vibration - part 1: General requirements, 1997.

ISO. 8608:2016, Mechanical vibration - Road surface profiles - reporting of measured data, 2016.

Raman K Mehra, Jayesh N Amin, Karl J Hedrick, Carlos Osorio, and Srinivasan Gopalasamy. Active suspension using preview information and model predictive control. In *Proceedings of the 1997 IEEE international conference on control applications*, pages 860–865. IEEE, 1997.

Jong Hyeon Park and Young Suk Kim. An h_∞ controlller for active suspensions and its robustness based on a full-car model. *IFAC Proceedings Volumes*, 32(2):8178–8183, 1999.

Wei Wang, Yan-Bing Xue, Yu-Ling Song, and Xiao-Chen Du. Fuzzy-pid control strategy for an active suspension based on optimal control laws with genetic algorithm. *Zhendong yu Chongji(Journal of Vibration and Shock)*, 31(22):157–162, 2012.

Nurkan Yagiz and Yuksel Hacioglu. Backstepping control of a vehicle with active suspensions. *Control Engineering Practice*, 16(12):1457–1467, 2008.

M Yu, C Cheng, S Evangelou, and D Dini. Robust control for a full-car prototype of series active variable geometry suspension. In *2019 IEEE 58th Conference on Decision and Control(CDC)*, 2019.

Min Yu, Carlos Arana, Simos A Evangelou, and Daniele Dini. Quarter-car experimental study for series active variable geometry suspension. *IEEE Transactions on Control Systems Technology*, 27(2):743–759, 2017.

Kemin Zhou and John Comstock Doyle. *Essentials of robust control*, volume 104. Prentice hall Upper Saddle River, NJ, 1998.